Atom Vacancies and Electronic Transmission Stark Effects in Boron Nanoflake Junctions

Journal:	*Journal of Materials Chemistry C*
Manuscript ID	TC-ART-07-2020-003116.R1
Article Type:	Paper
Date Submitted by the Author:	24-Jul-2020
Complete List of Authors:	Jones, Leighton; Northwestern University, Chemistry Mosquera, Martin; Northwestern University, Chemistry Schatz, George; Northwestern University, Chemistry Marks, Tobin; Northwestern University, Department of Chemistry Ratner, Mark; Northwestern University, Theoretical Chemistry

Atom Vacancies and Electronic Transmission Stark Effects in Boron Nanoflake Junctions

Leighton O. Jones, Martín A. Mosquera, George C. Schatz*, Tobin J. Marks*, Mark A. Ratner

Department of Chemistry and the Materials Research Center, Northwestern University, Evanston, IL-60208, USA.

KEYWORDS charge transport, stark effects, vacancies, nonlinear, boron, molecular junction, 2D materials.

ABSTRACT: Finite-sized boron nanomaterials have received little attention in comparison to their graphene-like 2D boron analogues. It is with systems of precise atomic structures where the electrical conductance can be most fruitfully analyzed at the fundamental level. To understand how conductance varies with respect to the electronic structure, and particularly with vacancies, we study finite-sized boron nanoflakes (BNFs) and closely examine their remarkable changes in physical properties. Unlike carbon-based materials, we find from non-equilibrium Green's functions density functional theory (NEGF-DFT) calculations that the charge transport of BNFs with 35-37 atoms is modulated by site-specific atomic vacancies. The BNF with no vacancy (B_{37}) shows significantly lower conductivity (9.23 μS), than B_{36} with one vacancy (46.1 μS), and lower still than with two vacancies (B_{35}, 54.2 μS). From the thermopower function, these nanomaterials change from strong hole conductors to electron and back to hole conductors with the addition of each vacancy, from a doublet (B_{37}) to singlet (B_{36}) to doublet (B_{35}) ground state, respectively. The projected density of states also reveals a trend from semiconducting to metallic-like character. A key finding is the observation of vacancy-dependent electronic transmission Stark effects (ETSEs) with respect to bias voltage (±1 V) in these molecular junctions. B_{37} exhibits quadratic behavior of resonance shifting, B_{36} shows competition between quadratic and cubic, and B_{35} exhibits a linear Stark effect, although this masks the nature of a cubic response at bias exceeding ±0.8 V. We prove that the vacancy position is a determining factor in the quadratic or linear ETSE behavior, from isomeric structures of these BNFs. The *I-V* responses also reveal that charge transport increases with vacancy for these nanoflakes. Thus, not only do vacancies affect nanoflake conductivity, but also the nature of electrical transmission in the presence of a voltage bias, which is important for transistor switching. It follows then, that rather than seeking to fabricate electronic devices with pristine, defect-free boron nanoflakes, we should, however, be introducing site-specific atomic defects for high-performance devices.

1. Introduction

Research over the last few decades has shown that boron can not only replicate typical carbon-based structures, from fullerenes[1,2] and nanotubes to 2D materials[3], but also yield materials that are exotic in both structure and properties[4], unlike any other element in the Periodic Table. For example, boron's unique multi-center bonding enables both typical inorganic clusters[5,6] and organic-like fragments[7]. The experimental observation of all-boron fullerenes[8], 2D borophene sheets[3,9] and nanoflakes[10,11] are now well reported.

Boron materials have wide-ranging applications including anticancer drug delivery systems[12], carbon dioxide capture[13], hydrogen storage[14], supercapacitors[15], lithium batteries and nanoplasmonics[16]. One interesting phenomenon is the correlation between structural stability and electrical properties in 2D materials. Defects, or more specifically atom vacancies, seemingly improve the charge transport properties, which is the inverse to normal carbon-based materials such as for graphene and nanotube devices[17].

There is a broad body of literature covering the electronic transport properties of boron materials. These include transmission in nanowires[18,19], nanocones[20], nanotubes[21], pristine borophene sheets[22] as well as hydrogen[23] and oxygen[24] surface defects in 2D boron. However, considering the intense interest in boron related technologies, there are limited reports on smaller molecular-scale structures, such as fullerenes[25,26] and a lithium hydride boron complex[14]; no pristine boron nanoflake studies (with or without vacancies) are available to the best of our knowledge, although high thermal conductivities have been reported[27].

Here we probe how atom vacancies affect the electrical transmission properties of boron nanoflakes. We chose to investigate finite-size nanoflakes to closely understand how these properties relate to the molecular nature of boron systems. Thus, a suitable molecule-sized structure is needed. Fortunately, boron fullerenes[2], clusters[28] and fragments[7,11] have gained considerable attention, particularly those of B_{35-37} nanoflakes[10] (Figure 1). From structural optimizations[29,30] and stability analysis[31,32], these were found to be stable and thus perfect candidates for our electrical transport investigations.

We build on this broad body of work and show in this contribution how the single and double vacancies can lead to an *increase* in conduction. We report the reorganization energies with respect to the spin-state of the nanoflakes. Using non-equilibrium

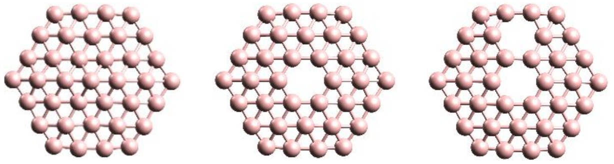

B_{37} B_{36} B_{35}

Figure 1. Three typical boron nanoflakes calculated to be stable[10]. The transmission and electronic properties of these structures and their isomers are investigated.

Green's functions density functional theory (NEGF-DFT) calculations, we also report on the exotic nature of the transmission spectra as a function of the eigenchannel around the Ohmic region, and detail the shift from an insulator-like nanoflake with no vacancies, exhibiting a quadratic Stark effect, to metallic-like species with two vacancies showing a cubic Stark effect. Finally, we also probe the thermopower functions for potential insights into realizing bias-dependent ambipolar switching devices.

2. Computational Methods

All structures were assembled in the open-source molecular editor software package Avogadro[33] (1.1.1). All structures were initially energy-minimized with a molecular mechanics Universal Force Field[34,35] (UFF) in Avogadro, which gives a good starting geometry for subsequent calculations at the quantum mechanical level. The resulting coordinates were optimized with quasi-Newton methods *via* quantum mechanics using Density Functional Theory (DFT).

The nanoflakes were first optimized in isolation with the hybrid-generalized gradient approximation (GGA) Becke three-parameter Lee–Yang– Parr (B3LYP) functional and the Pople double zeta with a polarization function 6-31G* basis, in the Northwest Computational Chemistry Package (NWChem). Vibrational calculations confirmed their ground state geometries. The internal hole and electron reorganization energies were computed according to the method in reference[36]. The method involves the calculation of the vertical ionization/vertical electron affinity to the respective cation/anion surfaces, followed by optimization of the cation and anion geometries. Then an electron is added to the cation/is removed from the anion in the remaining single point calculations to return to the neutral surface. The differences between the energies of the single point and the optimized cation geometry are labelled λ_1, and the energy difference between the electron affinity to the cation and the neutral surface is labelled λ_2. The sum of these two terms equals the hole reorganization energy, and the same approach is given to the electron reorganization energy.

These were subsequently optimized on a gold slab of three layers (111) with the Perdew–Burke–Ernzerhof (PBE) functional and a DZP basis, in the Spanish Initiative for Electronic Simulations with Thousands of Atoms (SIESTA[37], version 4.1-b3) program; using a k-grid size of 4×4×1 for the scatter region and 4×4×50 for the electrodes, a density matrix tolerance of 1.0×10^{-5} and a force tolerance of 0.05 eV $Å^{-1}$. Another slab was added to the other side of the molecule, and together with the former, now constitutes the scatter region. The structures in the scatter region were optimized once more at the PBE/DZP level.

B_{37} gave a relatively different optimized structure in the junction scatter region, in comparison with its isolated structure. A vibrational analysis was carried out on this structure and no negative frequencies were observed. No other optimized state could be found in the device region for B_{37}, thus this structure was used for transport calculations. The Cartesian coordinates of all species, including the isolated and junction structure B_{37}, are available in the SI.

The Green's functions for six layers of gold (111) were individually calculated for the left and right electrodes. The nuclear coordinates of these electrodes were subsequently added to either side of the scatter region, and collectively form the device. Charge transport, computed with the TranSiesta[38] program, was evaluated at the same level (PBE/DZP) for the transmission (PBE ultrasoft pseudopotentials). The resulting density matrix was post-processed with the tight-binding module (TB_{TRANS}) which is part of TranSiesta, giving the final transmission as a function of the selected voltage bias, across the eigenchannel. The bias-dependent current was calculated in the tunneling regime from the Landauer formula[39], the conductance was computed with the Landauer–non-equilibrium Green's function (NEGF) equation and the thermopower was calculated from the slope of the negative differential log of the transmission function; all methods are described in reference[40].

The electronic coupling was calculated using non-adiabatic electron hopping model from $D^- + A \rightarrow D + A^-$ where D and A are two neighboring BNF molecules. The molecular orbitals were relaxed in the presence of a negative charge using Frozen Density Embedding in the ADF program[41,42]. The transfer integrals were calculated based on the one-electron Hamiltonian of the fragment orbitals of D and A.

3. Results and Discussion

Structural properties such as bond lengths[28], binding energies[43,44], aromaticity[43,45,46], vibrational modes[2,29,45] and excited states[29] of all-boron materials have been extensively discussed in the literature. Here, we focus on a brief structural characterization of B_{35-37} nanoflakes in isolation and in a junction, followed by a detailed analysis of their electronic transport properties.

The BNFs have B-B bond lengths typical of boron nanomaterials which varies with respect to their nanoflake position both centrically and radially. B_{36} and analogues are reported[43] to have shared sigma 2c-2e, 3c-2e and 4c-2e B-B bonding between the outer, middle and inner rings. The π-electrons are described as extensively delocalized[10] 36c-2e bonds and the overall structures have concentric double aromaticity[46]. In general, we find the B-B bond distances range between 1.58 and 1.73 Å in the neutral ground states, depending on the measurement of the inner or outer rings and in agreement with boron clusters[47].

Discussion of doublet and triplet ground-state boron materials is limited in the literature, presented mostly for clusters[48–50], and warrants more detail for these promising materials. Due to the odd number of boron atoms for B_{37} and B_{35}, these two nanoflakes are doublets in their ground states, while B_{36} can be either singlet or triplet. For charge transfer, loss of an electron from B_{37}/B_{35} gives either singlet or triplet states (Figure 2A). The change to a triplet state (D→T) is energetically accessible with a relatively small penalty (< 1 eV) in comparison to the D→S process. The triplet ground state of B_{36} is higher in energy and has a lower vertical ionization energy (*IE*v) of 5.89 eV to the doublet state (T→D), than the more stable singlet to doublet transition (S→D) of 6.73 eV. Note that the triplet cations (and anions) of B_{37}/B_{35} are also relatively higher in energy than their singlet states. Similarly, the gain of an electron from the doublet states of B_{37}/B_{35} leads to either singlet or triplet states. The vertical electron affinities (*EA*v) 2.35-3.13 eV correlate with theoretical and experimental observations of boron nanoclusters[1,47]. In contrast to the ionization process, the formation of the ground-state triplet anion is lower (< 0.6 eV) than the ground-state singlet anion.

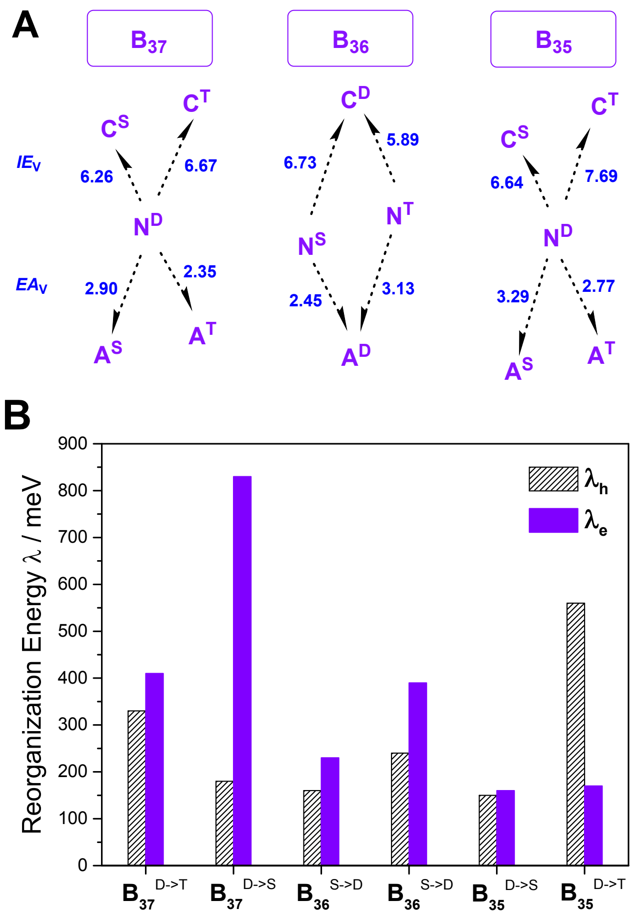

Figure 2. (**A**) Representations of spin states (singlet S, doublet D, triplet, T) of the isolated BNF neutral ground state (N) and charge transfer states (cation C, anion A). Levels not to scale, vertical ionization energy (IE_V) and vertical electron affinity (EA_V) are in eV. (**B**) Internal hole (λ_h) and electron (λ_e) reorganization energy (meV) of for the BNFs different CT spin states.

The measure of stability towards charge transfer for any molecular material is the internal reorganization energy[51], computed from the difference between the vertical and relaxed energy surfaces for holes and electrons (SI, Methods). Organic materials tend to be unstable towards charge injection, and ideal n-type materials are rare compared to p-type, with notable developments of non-fullerene acceptors[52]. However, electron-deficient elements doped into a material such as boron tend to be more stable towards negative charge. Boron-doped nanographenes[53] have a lower electron reorganization energy (λ_e) than hole (λ_h), on the order of 97 meV, however those of pure boron clusters, nanotubes and nanoflakes have yet to be investigated. Here, we find λ_e to be consistently higher than those of λ_h, for all charge transfer states except one, the λ_e (D→T)of B_{35} which is 170 meV in comparison to the λ_h (D→T) = 560 meV (Figure 2B). B_{35} also shows low λ_e =160 and λ_h = 150 meV for the D→S CT state, demonstrating that a BNF with two vacancies has an excellent propensity for CT. Low λ_h values are also observed for B_{37} (D→T) 180 meV and B_{36} (S→D) 160 meV.

Two sulfur atoms were added to the opposite corners of the BNFs, and along with the addition of two gold layers that constitute the scatter region. The sulfur atoms enable better contact with the gold surface, as is standard with typical molecular junctions[54] and the

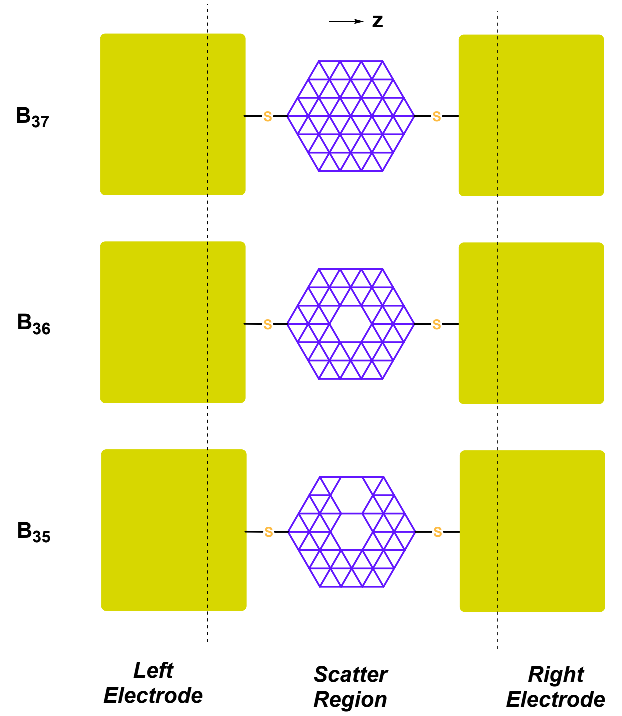

Figure 3. The BNF junctions, showing the orientation of the vacancy with respect to the z-direction (direction of transmission).

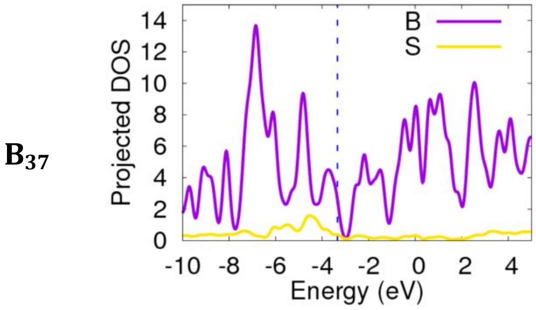

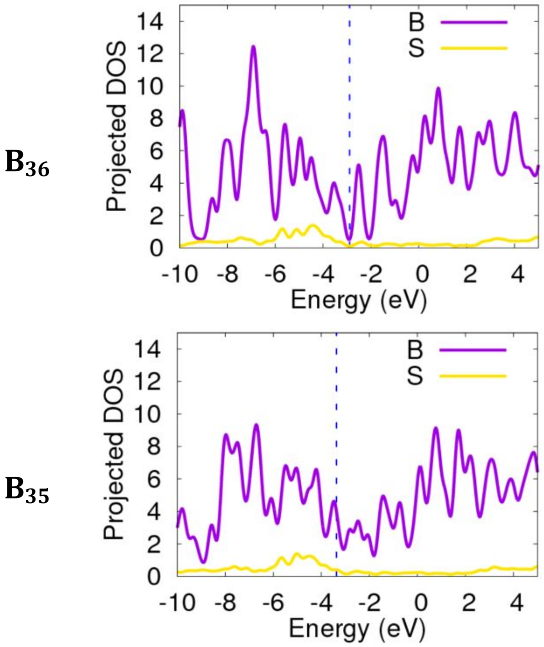

Figure 4. The projected density of states (DOS) for B (purple) and S (yellow) atoms for the nanoflakes in the scatter region (Au not showing).

inclusion of the gold layers reduces an incongruency in the chemical potential between the electrodes and the scatter region. The BNFs were further optimized and six layers of gold for the electrodes were added, completing the device (Figure 3). The corners of the BNFs were chosen to facilitate contact *via* the sulfur atoms with the electrodes to remove ambiguity about the path of current upon entering and exiting the BNFs. Therefore, all transmission results pertain to the remaining atoms within the BNF and not necessarily to edge states, although this can't be ruled out[55]. We note that interfacial hetero-junction type architectures are another possibility[56], where the BNFs could be stacked such that the gold layers are in contact with its surface and so the current would flow through the sheet rather than across it, but this is beyond the scope of this work.

The projected density of states (DOS) was computed for the scatter region only, and the high number of gold states are not shown due to saturation of the spectra. The Fermi level sits at the upper edge of one band in the B_{37} density of states spectrum (Figure 4). For B_{36}, the Fermi level sits in a gap, and the DOS for B_{35} is a continuous gapless spectrum. From these observations, we can expect semiconducting to metallic behavior across these three BNFs. The band gap of B_{37} correlates with carbon dot analogues[57], but the decreasing gaps of B_{36} and B_{35} are not so easily explained. It is interesting that the conductivity of graphene is found experimentally to increase with vacancies[58], as we observe with our BNFs (*vide infra*), yet the underpinning electronic details are not currently understood as to why this is the case. It could be that as the number of vacancies go up, the number of unbound states, or radicals also increases and results in population of the gap/conduction bands. Another option is metal-induced gap states[59] (MIGs), which can arise from strong coupling to the electrodes.

Next, we compute the electrical conductance of the ground states of these BNFs *via* NEGF-DFT using periodic DFT in the SIESTA program. The transmission spectra for each voltage bias

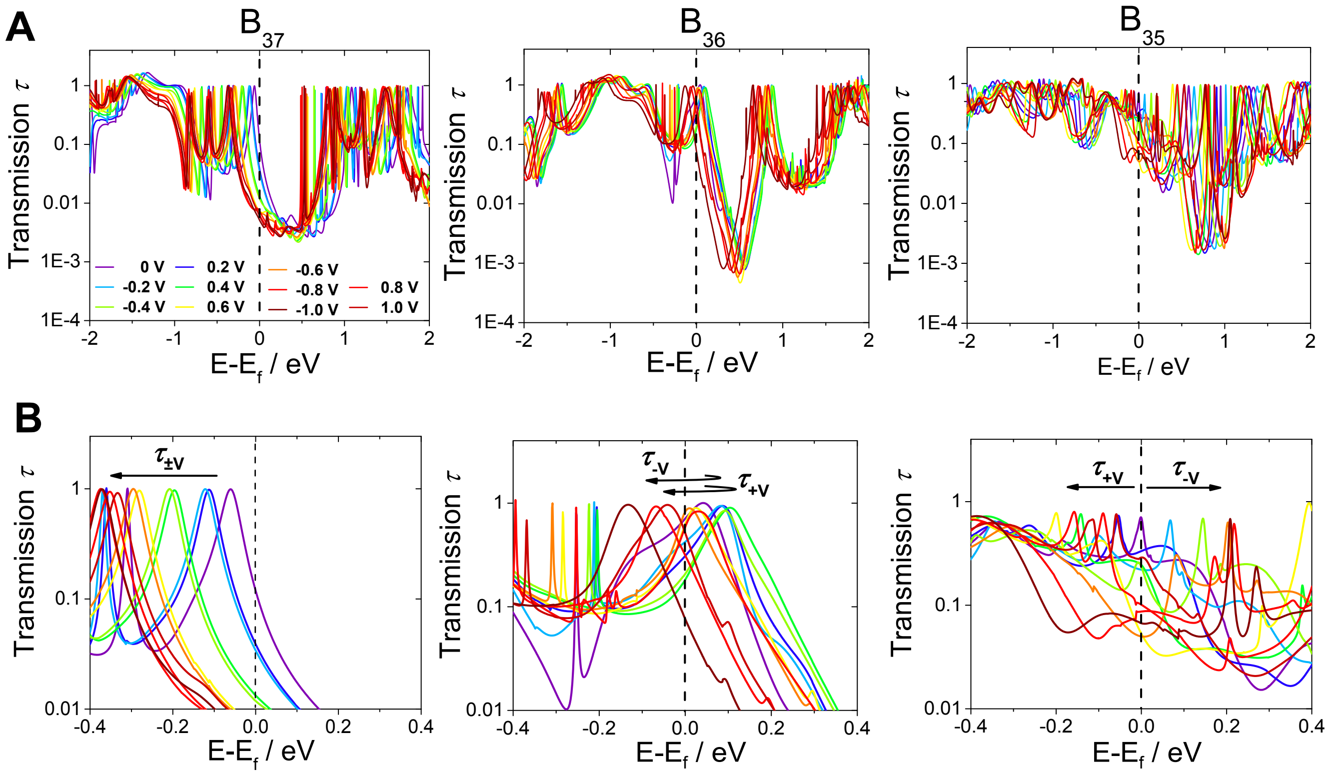

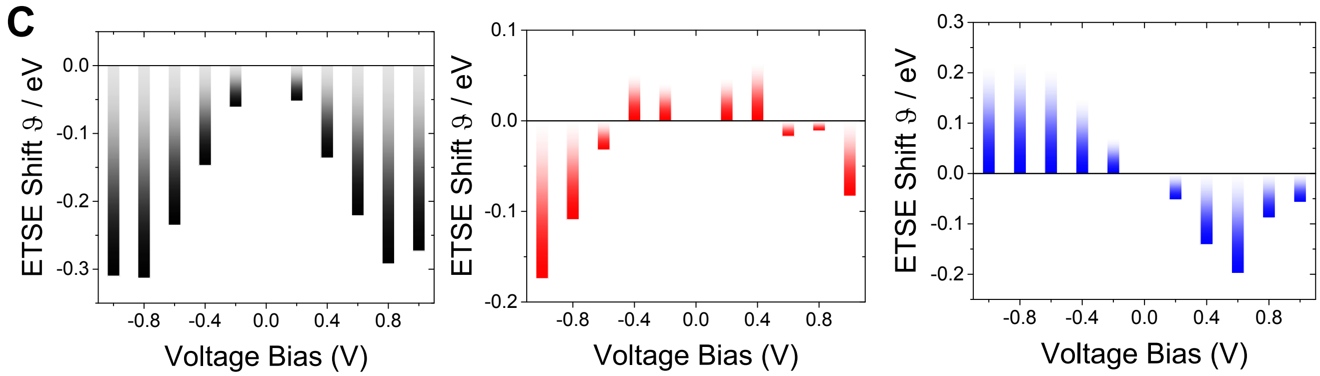

Figure 5. (**A**) Transmission spectra with respect to the Fermi level of B_{37}, B_{36} and B_{35} as a function of bias voltage on a logarithmic scale; (**B**) close-up view of the Ohmic region, showing the complex transmission shifting behavior across the Fermi level as a function of bias voltage (electronic transmission Stark effects, ETSEs); (**C**) ETSE shifts (ϑ/eV) of the resonance at the Fermi energy as a function of bias voltage and referenced to the resonance at zero bias.

between ±1 V are presented in Figure 5A. The Fermi level lies in a relatively wide resonance peak, the width of which increases with each added vacancy reflecting increased coupling to the electrodes[40]. From FWHM analysis[56] (Figure S7), we deduce the BNF-electrode coupling from the zero-bias resonance at the Fermi energy (from B_{37} to B_{35}) to be 0.103, 0.314 and 0.024 eV respectively. Deep valleys next to the resonances are observed with B_{37} and B_{36} in the unoccupied eigenchannels, but these disappear with B_{35}. The transmission for the BNFs increase with atom vacancy, from B_{37} ($\tau = 0.119$) having none, B_{36} ($\tau = 0.595$) with one and B_{35} ($\tau = 0.699$) with two. The transmission of B_{37} has similarities with the transmission function at the Fermi level of borophene, a 2D boron monolayer with H-atom substituents and no vacancies ($\tau < 0.1$), while those of B_{36} and B_{35} are similar to pristine borophene, which has vacancies ($\tau = \sim 0.7$)[60]. The electrical conductances increase from 9.23 μS to 54.2 μS, accordingly.

Upon inspection, the transmission for the BNFs appears to shift along the eigenchannel with respect to the voltage bias. This is indeed true, as found with a close-up view of the Ohmic region, clearly showing the shifting (Figure 5B). Such behavior is characteristic of a Stark effect. A Stark effect is the splitting of optical lines with an applied electric field. A first order (linear) Stark effect is the shifting in different directions (to higher or lower energies), and a quadratic Stark effect is the shifting in the same direction (either lower or higher energies). While optical and magnetic shifts are found commonly in a range of organic and inorganic materials[61,62], the shifting of an electric transmission spectrum with an applied voltage is rare, although we have previously observed this the electronic transmission Stark effect (ETSE) in carbon-based nanobelts[40]. To be clear, an ETSE relates to the electronic transmission of a molecular junction, which is not to be confused with common 'electronic' stark effects[63] in excited state absorption profiles (optical). ETSE adds to the known pool of constant-field (or direct-current, DC) Stark effects which include giant[64], excitonic[65], quantum-confined[66] and vibrational[67] effects; an AC equivalent is the Autler-Townes Stark effect in which the oscillation of a field changes an absorption lineshape[68]. There are numerous theoretical and experimental reports of *optical* Stark effects in boron-doped Si materials[69–71]. However, there are very limited reports of an electrical transmission shift with bias voltage (ETSEs) for boron materials, and those are by Yang *et al.*[25] who originally observed this with B_{40} clusters and ±0.8 V bias, but provided no analysis of this phenomena, and Dai *et al.*[72] present a linear electronic Stark effect with B_{40} clusters at a bias of 0.3 and 0.5 V. Similarly, we find the transmission spectra of the one-vacancy BNF B_{37} to shift to lower energies regardless of the size or sign of the bias (± 1V) and thus represents a quadratic ETSE. B_{36} shows complex behavior, but an overall trend to lower energies after an initial higher energy shift and appears to be competing between quadratic and cubic. Mixed-order Stark effects have also been observed in other elements, notably hydrogen[73]. Moreover, the two-vacancy nanoflake, B_{35}, shows a splitting of the spectra with respect to bias sign, which initially indicates a linear type ETSE. A positive bias moves the transmission spectra to negative eigenchannels, while a negative bias does the opposite. However, close inspection of the differences between the occupied channel resonances as shown in Figure 5B for B_{35} reveals non-equal displacements for ±0.8 and ±1.0 V, in agreement with findings by Yang[25], and are characteristic of cubic Stark effects[74] at these higher bias.

The ETSE shifts (ϑ/eV) for each bias voltage are determined from the displacement of the resonance at the Fermi energy, referenced to the same resonance at zero bias voltage. We find at a bias of +1 V, the ETSE shift for B_{37} is $\vartheta = -0.273$ eV and at -1 V, $\vartheta = -310$ eV; the negative sign implies the transmission shift is to a lower eigenvalue, while a positive sign is to a higher eigenvalue. Because the transmission results were calculated with respect to the Fermi energy, a shift to lower eigenvalue means the transmission occurs through lower occupied energy states, while a positive eigenvalue is the transmission through higher unoccupied states. The ETSEs of B_{37} within the ±1 V bias window are all negative, but this is not the case for the other two BNFs as shown in Figure 5C; the semi-linear ETSE shifts of B_{35} with cubic character are more clearly seen. The values of Figure 5C are presented in Table S2. Quantum-confined Stark effects of van der Waals heterojunctions[56] exhibit shifts of 0.021 eV, those of germanium quantum well structures 0.8 eV, while protein-coupled gold nanoclusters[75] range between 0.052 and 0.079 eV. One of the earlier studies[71] of B-doped Si observed Stark shifts between 0.06 and 0.1 eV. Depending on the bias, the ETSE shifts of these BNFs range between $|\vartheta| = 0.046$ to 0.310 eV, which are within the literature ranges.

It has been reported that the application of an electric field or a bias voltage decreases the gap of various materials[76,77] which correlates with the decreasing gap of the B_{37} to B_{35} structures studied here. Yet the exact relation to the atom vacancies is not clear. It was proposed that one possible origin for quadratic type optical Stark effects relates to the removal of degeneracies in excited states[71]. However, a linear Stark effect was observed by Calvet[69] with respect to bias voltage on a single atom impurity embedded in silicon. Moreover, we do not include excited state terms in our Landau transmission calculations, although the unoccupied levels are included when degeneracies may be affected by the vacancies. Linear Stark effects conventionally arise from molecules which possess a non-zero induced dipole moment, and a quadratic Stark effect with molecules that are symmetric[74]. We computed the dipoles and induced dipoles in an electric field (ensuring that the field values match those of the voltage bias). We find all three BNFs show a linear induced electric dipole across a 1 V window, stepped at ± 0.2 V $Å^{-1}$ (Figure S1-S3). B_{37} and B_{36} show similar trends for the individual x, y and z induced dipoles, while B_{35} exhibits opposite trends. Yet, the net induced dipoles are all relatively similar with no discernible differences. It should be noted that they all have dipoles in the absence of a field, with those of B_{37}, B_{36} and B_{35} being 0.95, 1.07 and 1.92 a.u. respectively, giving the relationship $B_{37} \sim B_{36} < B_{35}$. However, the trend is weak considering (1) the dipole of B_{35} is only double that of B_{37} and B_{36}; (2) 1.92 a.u. is relatively small yet comparable to other systems[78]. The interplay of bias-induced charging also modulates PCBM junctions[79] and CO-terminated Ag tips[80] between quadratic and linear, however our BNF junctions exhibit both quadratic and linear ETSEs across the bias voltage range. We also compute the induced polarizabilities (Figure S5) and for completeness, the relative dielectric constant[54] (Figure S6), and again the BNFs showcase similar behavior amongst themselves with no features that stand out.

Turning to the symmetry element in Stark effects, the

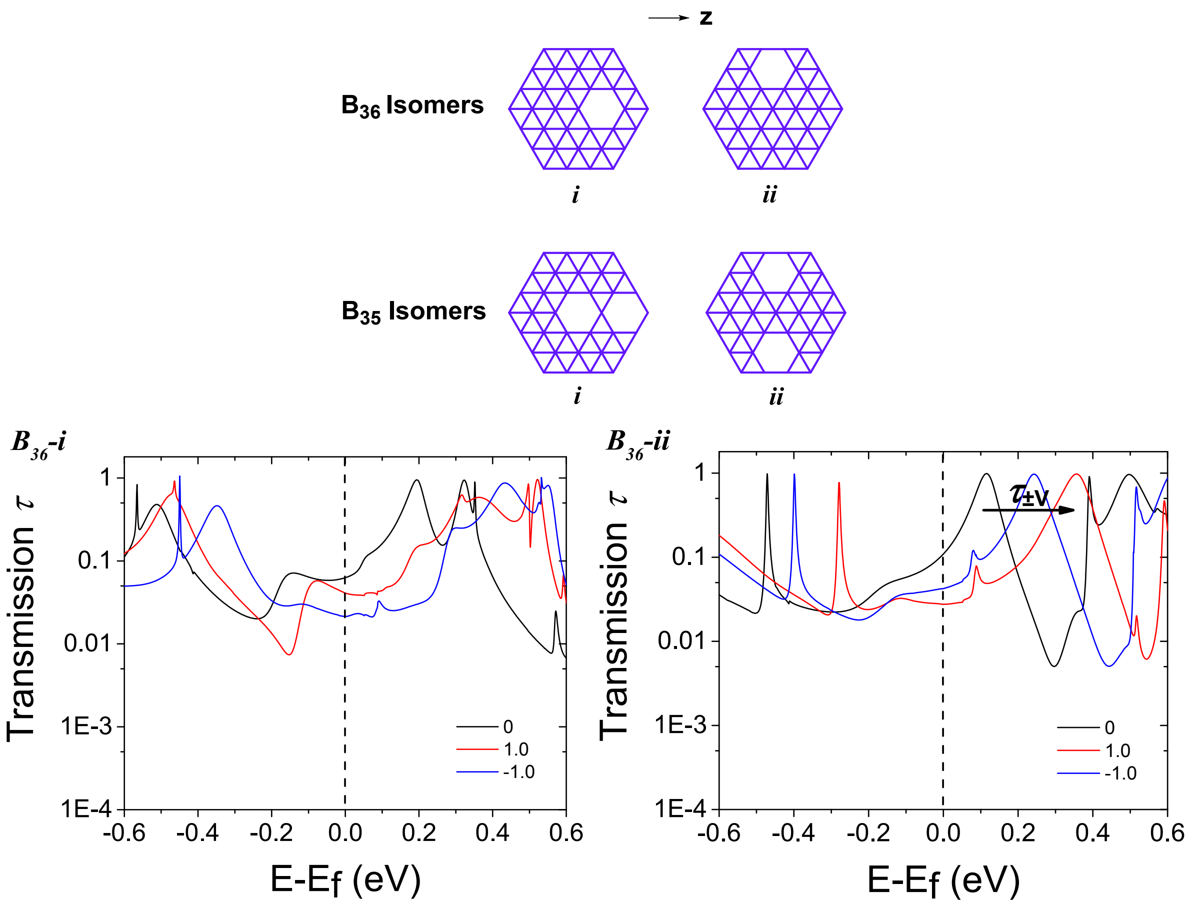

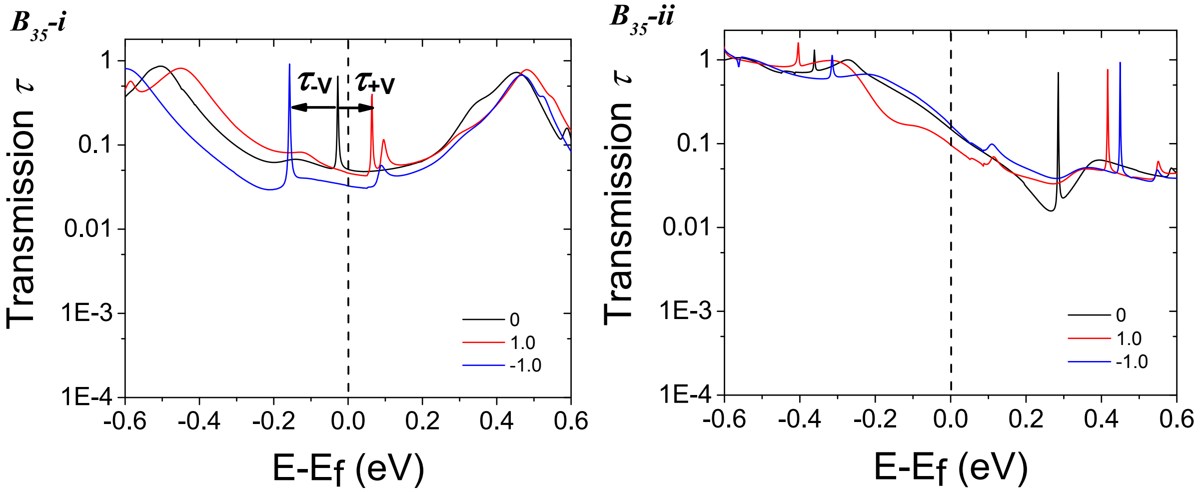

Figure 6. (Top) Selected isomeric structures of B_{36} and B_{35} in stick representation; their connection to the electrodes are in the horizontal (z-axis) direction, the same as those in Figure 3. (Bottom) Close-up view of the transmission spectra of those B_{36} and B_{35} isomers with respect to the Fermi level as a function of bias voltage on a logarithmic scale; a wider eigenvalue range is required due to resonances around ±0.4 eV .

orientation of the BNFs in our junctions are such that the B_{37} and B_{36} are symmetric in the z-direction, but the B_{35} is not. This is a clue as to the origins of the quadratic-to-linear ETSE. To determine whether or not the orientation of the vacancy with respect to the z-direction produces a quadratic or linear ETSE, we calculate the ±1 V bias transmissions of two isomers of B_{36} and B_{35}; the structures of these BNFs are shown in Figure 6 in stick representation, where each point represents a boron atom. These structures were selected such that one isomer for both B_{36} and B_{35} have their vacancies in line with the two sulfur contacts (B_{36}-*i* and B_{35}-*i*), so these should reproduce to some extent, the transmission and ETSE behavior of the parent structures (Figure 3). These vacancies were further arranged so that they are not in the direct path of current between the two sulfur connections (structures B_{36}-*ii* and B_{35}-*ii*) and should impart different behavior. It should be clarified that all these isomers were optimized in the junction so are at their energy minima.

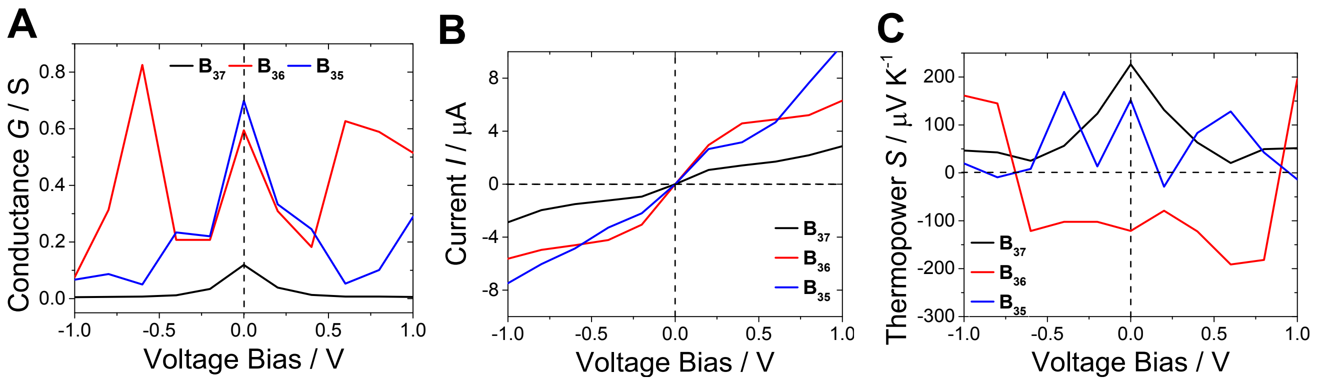

Figure 7. (**A**) Electrical conductivity; (**B**) *I*-*V* curves; (**C**) Thermopower function (*S*) with respect to bias voltage (V) at the Fermi energy for the indicated molecules. The dashed lines are to guide the eye only.

As expected, the transmission spectra for B_{36}-*i* reveals complex behavior which is symptomatic of the parent B_{36} structure. B_{35}-*i* shows clear linear ETSE, also akin to its B_{35} parent structure. The shifts are found to be $\vartheta = 0.092$ eV (+1 V) and -0.130 eV (-1 V). Interestingly, B_{36}-*ii* shows a quadratic ETSE, with shifts of $\vartheta = 0.241$ eV (+1 V) and 0.127 eV (-1 V), which is probably due to the flow of current unimpeded as the vacancy is above the horizontal path; this has a resemblance to the B_{37} structure and its transmission, except in this case, the quadratic effect is affecting the conduction channel. The transmission spectra of the B_{35}-*ii* structure show no discernible ETSE behavior, as the resonances around -0.4 eV appear to show a quadratic ETSE while those at 0.4 eV show linear, and thus are not easy to determine. From these spectra we can deduce that the position of the vacancies relative to the electrode contacts is a key factor in the generation of the linear, quadratic or mixed ETSEs.

Although the exact origin of the quadratic-to-linear ETSEs cannot be unambiguously ascertained, this study provides strong ground-work with the possibility that experimental observations will shed further light on their complex and exotic behavior. The importance, here, directly relates to the operation of boron-based molecular devices, whose electrical transmission will shift in the presence of an applied voltage bias, and thus, the conductance at the Fermi energy. We return to the analysis of the parent structures $B_{35\text{-}37}$, and find the electrical conductance *G* (units of quantum of conductance) of B_{37} to be relatively lower than the other two BNFs (Figure 7A). A maximum conductance for B_{36} was only reached at ±0.6 V, as the transmission resonance passes through the Fermi energy with increasing bias. B_{35} shows a similar but higher conductance profile than B_{37}.

The *I*-*V* relationships with bias voltage across a 2 V window (±1 V) was computed and is presented in Figure 7B. Note that all three molecules exhibit the characteristics of typical junction devices, some with notable performances. As expected, they behave as metals around the Ohmic region (±0.4 V), with B_{37} being the exception, followed closely by B_{35} at ±0.4 V. Thus, B_{37} gives an unimpressive response at high voltage bias (±1 V) and appears to be semiconductor-like. In contrast, at ±0.4 V, B_{36} reaches a plateau, and delivers a slightly elevated current at higher bias, while B_{35} has a mild inflection at ±0.4 V, before soaring with higher bias. This *I*-*V* response is in quantitative correlation with that of boron nanosheets[23] and boron nanotubes for gas sensors[81].

Next we consider the charge carrier type of these BNFs, which have received little attention in the literature[82] in comparison to other materials such as boron carbides[83,84]. The thermopower (Seebeck, *S*) function is a measure of the type of conduction, hole (p) or electron (n), and is the negative of the logarithmic derivative of the slope of the transmission function[85,86]. The thermopower of the present materials was computed as a function of bias voltage across a 2 V window (±1 V) and is presented in Figure 7C. It can be seen that the B_{36} nanoflake remains n-type across ±0.7 V, before shifting to p-type at higher bias of *ca.* 1 V. This abrupt change in charge carriers suggests applications in bias-dependent ambipolar switching. In contrast, the B_{37} remains entirely p-type across the window, with a maximum around the Fermi energy, as is correlated with the thermopower of borophane[82], while B_{35} has strong oscillations which largely remains p-type.

Lastly, we probe the potential for these BNFs to be used in applications such as in solid-state electronics or in van der Waals heterojunctions, by studying their electronic coupling between dimers stacked with a distance separation d_z (Å) spanning 6 Å. The electronic coupling was calculated with a non-adiabatic electron hopping model using Frozen Density Embedding in the ADF program[41,42]. Although many permutations of the BNFs intermolecular positions with respect to each other are conceivable, such as slipped-stacking and herring-bone, we limit the scope to the z-axis. Remarkably, we find that the electronic coupling of the BNFs exceeds that of the latest carbon-based non-fullerene acceptors[52], by an order of magnitude. This is due to (1) the atomic radius of boron is greater than carbon and (2) the boron orbitals are more diffuse due to lower electronegativity. Figure 8 shows that the coupling

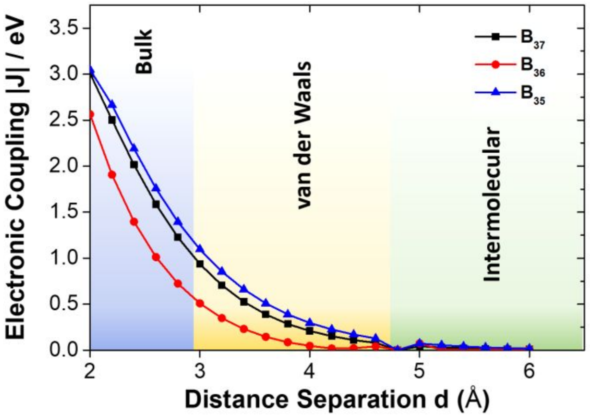

Figure 8. Electronic coupling |*J*| of cofacial BNF dimers as a function of separation d_z (Å).

between dimers of B_{36} molecules is the weakest in comparison to the B_{37} and B_{35} dimers since these molecules are doublets, each with an unpaired electron which can extend and interact further. The |*J*| coupling for B_{35} is the largest, for all separations, but the exact origin is unclear. Even at the separation of typical aromatic carbon π-π interactions, such as 3.4 Å, where |*J*| = 0.057 eV[42], we find the BNF coupling to be an order of magnitude larger, |*J*| = 0.52 eV for B_{37} and |*J*| = 0.66 for B_{35}. Even at 5 Å, the couplings for all three BNFs range between |*J*| = 0.04-0.07 eV. This result showcases the strength of the intermolecular cofacial coupling for boron-based nanoflake materials and their potential for applications in electronic devices.

4. Conclusions

An in-depth study of the electronic structures and transport properties of a closely-related series of three BNFs is reported, with striking findings. We observe that (1) the BNFs show varied electrical transmission Stark effects as a function of both atom vacancy and voltage bias, from quadratic (B_{37}) to linear (B_{35}) with mixed behavior from B_{36}; (2) the I-V response from B_{37} reveals the weakest conductance out of the three, and is on par with defect-free boron sheets being lower than defect-containing sheets; (3) the largest conductance arises from the nanoflake having a single vacancy (B_{36}) with n-type behavior, while the other two are p-type, (4) their intermolecular electronic coupling integrals of the BNFs exceed the largest coupling of the organic non-fullerene acceptors by an order of magnitude. These results can aid experimental findings by rationalization of the electronic structures and transport phenomena, and the design of advanced materials, while also contributing to the toolbox of molecular engineering for boron-based nano devices.

Conflicts of Interest

The authors declare no conflict of interest.

Acknowledgements

LOJ and GCS acknowledge support from the LEAP center at Northwestern University, sponsored by the Department of Energy, Office of Basic Energy Science, under grant DE-SC0001059; MAM and MAR acknowledge support from the Department of Energy, grant DE-AC02-06CH11357; TJM thanks Northwestern University MRSEC (NSF grant DMR-1720139) for support. This research was also supported in part through the computational resources and staff contributions provided for the Quest high performance computing facility at Northwestern University which is jointly supported by the Office of the Provost, the Office for Research, and Northwestern University Information Technology.

References

(1) Chopra, S. Boron Fullerenes, Bn (N=20, 30, 38, 40, 50, 60): First Principle Calculations of Electronic and Optical Properties. *J. Mol. Graph. Model.* **2018**, *84*, 90–95.

(2) Baruah, T.; Pederson, M. R.; Zope, R. R. Vibrational Stability and Electronic Structure of a B 80 Fullerene. *Phys. Rev. B* **2008**, *78* (4), 045408.

(3) Feng, B.; Zhang, J.; Zhong, Q.; Li, W.; Li, S.; Li, H.; Cheng, P.; Meng, S.; Chen, L.; Wu, K. Experimental Realization of Two-Dimensional Boron Sheets. *Nat. Chem.* **2016**, *8* (6), 563–568.

(4) and, J. E. F.; Ugalde, J. M. The Curiously Stable Cluster and Its Neutral and Anionic Counterparts: The Advantages of Planarity†. **1999**.

(5) Chen, Q.; Li, W.-L.; Zhao, X.-Y.; Li, H.-R.; Feng, L.-Y.; Zhai, H.-J.; Li, S.-D.; Wang, L.-S. B $_{33}^{-}$ and B $_{34}^{-}$: Aromatic Planar Boron Clusters with a Hexagonal Vacancy. *Eur. J. Inorg. Chem.* **2017**, *2017* (38–39), 4546–4551.

(6) Oger, E.; Crawford, N. R. M.; Kelting, R.; Weis, P.; Kappes, M. M.; Ahlrichs, R. Boron Cluster Cations: Transition from Planar to Cylindrical Structures. *Angew. Chemie Int. Ed.* **2007**, *46* (44), 8503–8506.

(7) Sergeeva, A. P.; Piazza, Z. A.; Romanescu, C.; Li, W.-L.; Boldyrev, A. I.; Wang, L.-S. B $_{22}^{-}$ and B $_{23}^{-}$: All-Boron Analogues of Anthracene and Phenanthrene. *J. Am. Chem. Soc.* **2012**, *134* (43), 18065–18073.

(8) Zhai, H.-J.; Zhao, Y.-F.; Li, W.-L.; Chen, Q.; Bai, H.; Hu, H.-S.; Piazza, Z. A.; Tian, W.-J.; Lu, H.-G.; Wu, Y.-B.; et al. Observation of an All-Boron Fullerene. *Nat. Chem.* **2014**, *6* (8), 727–731.

(9) Dellasega, D.; Russo, V.; Pezzoli, A.; Conti, C.; Lecis, N.; Besozzi, E.; Beghi, M.; Bottani, C. E.; Passoni, M. Boron Films Produced by High Energy Pulsed Laser Deposition. *Mater. Des.* **2017**, *134*, 35–43.

(10) Piazza, Z. A.; Hu, H.-S.; Li, W.-L.; Zhao, Y.-F.; Li, J.; Wang, L.-S. Planar Hexagonal B36 as a Potential Basis for Extended Single-Atom Layer Boron Sheets. *Nat. Commun.* **2014**, *5* (1), 3113.

(11) Sergeeva, A. P.; Zubarev, D. Y.; Zhai, H.-J.; Boldyrev, A. I.; Wang, L.-S. A Photoelectron Spectroscopic and Theoretical Study of B $_{16}^{-}$ and B $_{16}^{2-}$: An All-Boron Naphthalene. *J. Am. Chem.*

Soc. **2008**, *130* (23), 7244–7246.

(12) Shakerzadeh, E. Quantum Chemical Assessment of the Adsorption Behavior of Fluorouracil as an Anticancer Drug on the B36 Nanosheet. *J. Mol. Liq.* **2017**, *240*, 682–693.

(13) Tan, X.; Tahini, H. A.; Smith, S. C. Borophene as a Promising Material for Charge-Modulated Switchable CO $_2$ Capture. *ACS Appl. Mater. Interfaces* **2017**, *9* (23), 19825–19830.

(14) Liu, C.-S.; Wang, X.; Ye, X.-J.; Yan, X.; Zeng, Z. Curvature and Ionization-Induced Reversible Hydrogen Storage in Metalized Hexagonal B $_{36}$. *J. Chem. Phys.* **2014**, *141* (19), 194306.

(15) Zhan, C.; Zhang, P.; Dai, S.; Jiang, D. Boron Supercapacitors. *ACS Energy Lett.* **2016**, *1* (6), 1241–1246.

(16) Huang, Y.; Shirodkar, S. N.; Yakobson, B. I. Two-Dimensional Boron Polymorphs for Visible Range Plasmonics: A First-Principles Exploration. *J. Am. Chem. Soc.* **2017**, *139* (47), 17181–17185.

(17) Balasubramanian, K.; Burghard, M.; Kern, K.; Scolari, M.; Mews, A. Photocurrent Imaging of Charge Transport Barriers in Carbon Nanotube Devices. *Nano Lett.* **2005**, *5* (3), 507–510.

(18) Wang, D.; Lu, J. G.; Otten, C. J.; Buhro, W. E. Electrical Transport in Boron Nanowires. *Appl. Phys. Lett.* **2003**.

(19) Liu, F.; Tian, J.; Bao, L.; Yang, T.; Shen, C.; Lai, X.; Xiao, Z.; Xie, W.; Deng, S.; Chen, J.; et al. Fabrication of Vertically Aligned Single-Crystalline Boron Nanowire Arrays and Investigation of Their Field-Emission Behavior. *Adv. Mater.* **2008**.

(20) Wang, X.; Tian, J.; Yang, T.; Bao, L.; Hui, C.; Liu, F.; Shen, C.; Gu, C.; Xu, N.; Gao, H. Single Crystalline Boron Nanocones: Electric Transport and Field Emission Properties. *Adv. Mater.* **2007**.

(21) Bezugly, V.; Kunstmann, J.; Grundkötter-Stock, B.; Frauenheim, T.; Niehaus, T.; Cuniberti, G. Highly Conductive Boron Nanotubes: Transport Properties, Work Functions, and Structural Stabilities. *ACS Nano* **2011**.

(22) Adamska, L.; Sadasivam, S.; Foley, J. J.; Darancet, P.; Sharifzadeh, S. First-Principles Investigation of Borophene as a Monolayer Transparent Conductor. *J. Phys. Chem. C* **2018**, *122* (7), 4037–4045.

(23) Sun, J.; Zhang, Y.; Leng, J.; Ma, H. The Electronic and Transport Properties of Borophane with Defects: A First Principles Study. *Phys. E Low-dimensional Syst. Nanostructures* **2018**, *97*, 170–176.

(24) He, Y.; Cheng, N.; Chen, C.; Xiong, S.; Zhao, J. Tuning the Electronic Transport Anisotropy in Borophene via Oxidation Strategy. *Sci. China Technol. Sci.* **2019**, *62* (5), 799–810.

(25) Yang, Z.; Ji, Y. L.; Lan, G.; Xu, L. C.; Liu, X.; Xu, B. Design Molecular Rectifier and Photodetector with All-Boron Fullerene. *Solid State Commun.* **2015**.

(26) He, H.; Pandey, R.; Boustani, I.; Karna, S. P. Metal-like Electrical Conductance in Boron Fullerenes. *J. Phys. Chem. C* **2010**.

(27) Mortazavi, B.; Makaremi, M.; Shahrokhi, M.; Raeisi, M.; Singh, C. V.; Rabczuk, T.; Pereira, L. F. C. Borophene Hydride: A Stiff 2D Material with High Thermal Conductivity and Attractive Optical and Electronic Properties. *Nanoscale* **2018**, *10* (8), 3759–3768.

(28) Li, Q. S.; Jin, Q.; Luo, Q.; Tang, A. C.; Yu, J. K.; Zhang, H. X. Structure and Stability of B6, B+6, and B?6 Clusters. *Int. J. Quantum Chem.* **2003**, *94* (5), 269–278.

(29) Xu, S.; Dong, R.; Lv, C.; Wang, C.; Cui, Y. Configurations and Characteristics of Boron and B36 Clusters. *J. Mol. Model.* **2017**, *23* (7), 198.

(30) Chen, X.; Zhao, Y.-F.; Wang, L.-S.; Li, J. Recent Progresses of Global Minimum Searches of Nanoclusters with a Constrained Basin-Hopping Algorithm in the TGMin Program. *Comput. Theor. Chem.* **2017**, *1107*, 57–65.

(31) Shekaari, A.; Jafari, M. Finite Temperature Properties and Phase Transition Behavior of Quasi-Planar B $_{36}$ Nanocluster from First Principles. *Mater. Res. Express* **2018**, *6* (2), 025014.

(32) Xu, S.-G.; Zhao, Y.-J.; Yang, X.-B.; Xu, H. A Practical Criterion for Screening Stable Boron Nanostructures. *J. Phys. Chem. C* **2017**, *121* (21), 11950–11955.

(33) Hanwell, M. D.; Curtis, D. E.; Lonie, D. C.; Vandermeersch, T.; Zurek, E.; Hutchison, G. R. Avogadro: An Advanced Semantic Chemical Editor, Visualization, and Analysis Platform. *J. Cheminform.* **2012**, *4* (1), 17.

(34) Rappe, A. K.; Casewit, C. J.; Colwell, K. S.; Goddard, W. A.; Skiff, W. M. UFF, a Full Periodic Table Force Field for Molecular Mechanics and Molecular Dynamics Simulations. *J. Am. Chem. Soc.* **1992**, *114* (25), 10024–10035.

(35) Rappe, A. K.; Colwell, K. S.; Casewit, C. J. Application of a Universal Force Field to Metal Complexes. *Inorg. Chem* **1993**, *32*, 3438–3450.

(36) Jones, L.; Lin, L. A Theoretical Study on the Isomers of the B5TB Heteroacene for Improved Semiconductor Properties in Organic Electronics. *Comput. Theor. Chem.* **2017**, *1115*, 22–29.

(37) Soler, J. M.; Artacho, E.; Gale, J. D.; García, A.; Junquera, J.; Ordejón, P.; Sánchez-Portal, D. The SIESTA Method for *Ab Initio* Order- *N* Materials Simulation. *J. Phys. Condens. Matter* **2002**, *14* (11), 2745–2779.

(38) Papior, N.; Lorente, N.; Frederiksen, T.; García, A.; Brandbyge, M. Improvements on Non-Equilibrium and Transport Green Function Techniques: The next-Generation Transiesta. *Comput. Phys. Commun.* **2017**, *212*, 8–24.

(39) Famili, M.; Grace, I. M.; Al-Galiby, Q.; Sadeghi, H.; Lambert, C. J. Toward High Thermoelectric Performance of Thiophene and Ethylenedioxythiophene (EDOT) Molecular Wires. *Adv. Funct. Mater.* **2018**, *28* (15), 1703135.

(40) Jones, L. O.; Mosquera, M. A.; Schatz, G. C.; Ratner, M. A. Charge Transport and Thermoelectric Properties of Carbon Sulfide Nanobelts in Single-Molecule Sensors. *Chem. Mater.* **2019**, acs.chemmater.8b05119.

(41) Jacob, C. R.; Neugebauer, J.; Visscher, L. Software News and Update a Flexible Implementation of Frozen-Density Embedding for Use in Multilevel Simulations. *J. Comput. Chem.* **2008**, *29* (6), 1011–1018.

(42) Swick, S. M.; Alzola, J. M.; Sangwan, V. K.; Amsterdam, S. H.; Zhu, W.; Jones, L. O.; Powers-Riggs, N.; Facchetti, A.; Kohlstedt, K. L.; Schatz, G. C.; et al. Fluorinating Π-Extended Molecular Acceptors Yields Highly Connected Crystal Structures and Low Reorganization Energies for Efficient Solar Cells. *Adv. Energy Mater.* **2020**, *10* (23), 2000635.

(43) Chen, Q.; Wei, G.-F.; Tian, W.-J.; Bai, H.; Liu, Z.-P.; Zhai, H.-J.; Li, S.-D. Quasi-Planar Aromatic B $_{36}$ and B $_{36}^{-}$ Clusters: All-Boron Analogues of Coronene. *Phys. Chem. Chem. Phys.* **2014**, *16* (34), 18282.

(44) Li, W.-L.; Chen, Q.; Tian, W.-J.; Bai, H.; Zhao, Y.-F.; Hu, H.-S.; Li, J.; Zhai, H.-J.; Li, S.-D.; Wang, L.-S. The B $_{35}$ Cluster with a Double-Hexagonal Vacancy: A New and More Flexible Structural Motif for Borophene. *J. Am. Chem. Soc.* **2014**, *136* (35), 12257–12260.

(45) Rzepa, H. S. The Distortivity of π-Electrons in Conjugated Boron Rings. *Phys. Chem. Chem. Phys.* **2009**, *11* (43), 10042.

(46) Li, R.; You, X.-R.; Wang, K.; Zhai, H.-J. Nature of Bonding in Bowl-Like B $_{36}$ Cluster Revisited: Concentric (6π+18π) Double Aromaticity and Reason for the Preference of a Hexagonal Hole in a Central Location. *Chem. - An Asian J.* **2018**, *13* (9), 1148–1156.

(47) Akman, N.; Tas, M.; Özdoğan, C.; Boustani, I. Ionization Energies, Coulomb Explosion, Fragmentation, Geometric, and Electronic Structures of Multicharged Boron Clusters B n (n = 2–13). *Phys. Rev. B* **2011**, *84* (7), 075463.

(48) Zhai, H.-J.; Kiran, B.; Li, J.; Wang, L.-S. Hydrocarbon Analogues of Boron Clusters — Planarity, Aromaticity and Antiaromaticity. *Nat. Mater.* **2003**, *2* (12), 827–833.

(49) Alexandrova, A. N.; Boldyrev, A. I.; Zhai, H.-J.; Wang, L.-S. Electronic Structure, Isomerism, and Chemical Bonding in B 7 - and B 7. *J. Phys. Chem. A* **2004**, *108* (16), 3509–3517.

(50) Liao, Y.; Cruz, C. L.; von Ragué Schleyer, P.; Chen, Z. Many M©Bn Boron Wheels Are Local, but Not Global Minima. *Phys. Chem. Chem. Phys.* **2012**, *14* (43), 14898.

(51) Jones, L.; Lin, L.; Chamberlain, T. W. Oxygen, Sulfur and Selenium Terminated Single-Walled Heterocyclic Carbon Nanobelts (SWHNBs) as Potential 3D Organic Semiconductors. *Nanoscale* **2018**, *10* (16), 7639–7648.

(52) Swick, S.; Gebraad, T.; Jones, L.; Fu, B.; Aldrich, T.; Kohlstedt, K.; Schatz, G.; Facchetti, A.; Marks, T. Building Blocks for High-Efficiency Organic Photovoltaics. Interplay of Molecular, Crystal, and Electronic Properties of Post-Fullerene ITIC Ensembles. *ChemPhysChem* **2019**.

(53) Irfan, A.; Chaudhry, A. R.; Muhammad, S.; Al-Sehemi, A. G. Exploring the Potential of Boron-Doped Nanographene as Efficient Charge Transport and Nonlinear Optical Material: A First-Principles Study. *J. Mol. Graph. Model.* **2017**, *75*, 209–219.

(54) Jones, L. O.; Mosquera, M. A.; Fu, B.; Schatz, G. C.; Marks, T. J.; Ratner, M. A. Quantum Interference and Substantial Property Tuning in Conjugated *Z - Ortho* -Regio-Resistive Organic (ZORRO) Junctions. *Nano Lett.* **2019**, *19* (12), 8956–8963.

(55) Lin, C. K. Theoretical Study of Graphene Nanoflakes with Nitrogen and Vacancy Defects: Effects of Flake Sizes and Defect Types on Electronic Excitation Properties. *J. Phys. Chem. C* **2015**, *119* (48), 27131–27144.

(56) Chakraborty, C.; Goodfellow, K. M.; Dhara, S.; Yoshimura, A.; Meunier, V.; Vamivakas, A. N. Quantum-Confined Stark Effect of Individual Defects in a van Der Waals Heterostructure. *Nano Lett.* **2017**, *17* (4), 2253–2258.

(57) Xu, Q.; Liu, Y.; Gao, C.; Wei, J.; Zhou, H.; Chen, Y.; Dong, C.; Sreeprasad, T. S.; Li, N.; Xia, Z. Synthesis, Mechanistic Investigation, and Application of Photoluminescent Sulfur and Nitrogen Co-Doped Carbon Dots. *J. Mater. Chem. C* **2015**, *3* (38), 9885–9893.

(58) Jafri, S. H. M.; Carva, K.; Widenkvist, E.; Blom, T.; Sanyal, B.; Fransson, J.; Eriksson, O.; Jansson, U.; Grennberg, H.; Karis, O.; et al. Conductivity Engineering of Graphene by Defect Formation. *J. Phys. D. Appl. Phys.* **2010**, *43* (4), 045404.

(59) Archambault, C.; Rochefort, A. States Modulation in Graphene Nanoribbons through Metal Contacts. *ACS Nano* **2013**, *7* (6), 5414–5420.

(60) Padilha, J. E.; Miwa, R. H.; Fazzio, A. Directional Dependence of the Electronic and Transport Properties of 2D Borophene and Borophane. *Phys. Chem. Chem. Phys.* **2016**.

(61) Pearson, E. F.; Norris, C. L.; Flygare, W. H. Molecular Zeeman Effect, Electric Dipole Moment, and Boron Nuclear Hyperfine Coupling Constants in HBS. *J. Chem. Phys.* **1974**.

(62) Kuo, Y.-H.; Lee, Y. K.; Ge, Y.; Ren, S.; Roth, J. E.; Kamins, T. I.; Miller, D. A. B.; Harris, J. S. Strong Quantum-Confined Stark Effect in Germanium Quantum-Well Structures on Silicon. *Nature* **2005**, *437* (7063), 1334–1336.

(63) Gurav, N. D.; Gejji, S. P.; Pathak, R. K. Electronic Stark Effect for a Single Molecule: Theoretical UV Response. *Comput. Theor. Chem.* **2018**, *1138*, 23–38.
(64) Liu, Y.; Qiu, Z.; Carvalho, A.; Bao, Y.; Xu, H.; Tan, S. J. R.; Liu, W.; Castro Neto, A. H.; Loh, K. P.; Lu, J. Gate-Tunable Giant Stark Effect in Few-Layer Black Phosphorus. *Nano Lett.* **2017**, *17* (3), 1970–1977.
(65) Combescot, M.; Combescot, R. Excitonic Stark Shift: A Coupling to "Semivirtual" Biexcitons. *Phys. Rev. Lett.* **1988**, *61* (1), 117–120.
(66) Roch, J. G.; Leisgang, N.; Froehlicher, G.; Makk, P.; Watanabe, K.; Taniguchi, T.; Schönenberger, C.; Warburton, R. J. Quantum-Confined Stark Effect in a MoS $_2$ Monolayer van Der Waals Heterostructure. *Nano Lett.* **2018**, *18* (2), 1070–1074.
(67) Fried, S. D.; Boxer, S. G. Measuring Electric Fields and Noncovalent Interactions Using the Vibrational Stark Effect. *Acc. Chem. Res.* **2015**, *48* (4), 998–1006.
(68) Autler, S. H.; Townes, C. H. Stark Effect in Rapidly Varying Fields. *Phys. Rev.* **1955**, *100* (2), 703–722.
(69) Calvet, L. E.; Wheeler, R. G.; Reed, M. A. Observation of the Linear Stark Effect in a Single Acceptor in Si. *Phys. Rev. Lett.* **2007**.
(70) Smit, G. D. J.; Rogge, S.; Caro, J.; Klapwijk, T. M. Stark Effect in Shallow Impurities in Si. *Phys. Rev. B - Condens. Matter Mater. Phys.* **2004**.
(71) White, J. J. Effects of External and Internal Electric Fields on the Boron Acceptor States in Silicon. *Can. J. Phys.* **1967**, *45* (8), 2695–2718.
(72) Dai, X.; Zhou, Y.; Li, J.; Zhang, L.; Zhao, Z.; Li, H. Electronic Transport Properties of Single-Wall Boron Nanotubes. *Chinese Phys. B* **2017**.
(73) Blashenkov, N. M.; Lavrent'ev, G. Y. Optical Radiation and Ionization of Hydrogen Atoms in Heterogeneous Exothermal Reactions Proceeding in an Electric Field. *Tech. Phys.* **2009**, *54* (9), 1368–1371.
(74) Latychevskaia, T. Y.; Renn, A.; Wild, U. P. Higher-Order Stark Effect on Single-Molecules. *Chem. Phys.* **2002**, *282* (1), 109–119.
(75) Wen, X.; Yu, P.; Toh, Y. R.; Tang, J. Quantum Confined Stark Effect in Au8 and Au25 Nanoclusters. *J. Phys. Chem. C* **2013**, *117* (7), 3621–3626.
(76) Talla, J. A. Band Gap Tuning of Defective Silicon Carbide Nanotubes under External Electric Field: Density Functional Theory. *Phys. Lett. Sect. A Gen. At. Solid State Phys.* **2019**, *383* (17), 2076–2081.
(77) An, W.; Wu, X.; Zeng, X. C. Effect of Apical Defects and Doped Atoms on Field Emission of Boron Nitride Nanocones. *J. Phys. Chem. B* **2006**, *110* (33), 16346–16352.
(78) Wasileski, S. A.; Koper, M. T. M.; Weaver, M. J. Field-Dependent Electrode-Chemisorbate Bonding: Sensitivity of Vibrational Stark Effect and Binding Energetics to Nature of Surface Coordination. *J. Am. Chem. Soc.* **2002**, *124* (11), 2796–2805.
(79) Li, Y.; Zolotavin, P.; Doak, P.; Kronik, L.; Neaton, J. B.; Natelson, D. Interplay of Bias-Driven Charging and the Vibrational Stark Effect in Molecular Junctions. *Nano Lett.* **2016**, *16* (2), 1104–1109.
(80) Gieseking, R. L. M.; Lee, J.; Tallarida, N.; Apkarian, V. A.; Schatz, G. C. Bias-Dependent Chemical Enhancement and Nonclassical Stark Effect in Tip-Enhanced Raman Spectromicroscopy of CO-Terminated Ag Tips. *J. Phys. Chem. Lett.* **2018**, *9* (11), 3074–3080.
(81) Bhuvaneswari, R.; Chandiramouli, R. DFT Investigation on the Adsorption Behavior of Dimethyl and Trimethyl Amine Molecules on Borophene Nanotube. *Chem. Phys. Lett.* **2018**.
(82) Zare, M. Thermoelectric Transport Properties of Borophane. *Phys. Rev. B* **2019**.
(83) Mori, T.; Nishimura, T.; Yamaura, K.; Takayama-Muromachi, E. High Temperature Thermoelectric Properties of a Homologous Series of n -Type Boron Icosahedra Compounds: A Possible Counterpart to p -Type Boron Carbide. In *Journal of Applied Physics*; 2007.
(84) Aselage, T. L.; McCready, S. S.; Emin, D. Conductivities and Seebeck Coefficients of Boron Carbides: Softening Bipolaron Hopping. *Phys. Rev. B - Condens. Matter Mater. Phys.* **2001**.
(85) Lee, S. K.; Ohto, T.; Yamada, R.; Tada, H. Thermopower of Benzenedithiol and C $_{60}$ Molecular Junctions with Ni and Au Electrodes. *Nano Lett.* **2014**, *14* (9), 5276–5280.
(86) Karlström, O.; Strange, M.; Solomon, G. C. Understanding the Length Dependence of Molecular Junction Thermopower. *J. Chem. Phys.* **2014**, *140* (4), 044315.

SYNOPSIS TOC